

Structure-Property Relationships in Conventional and Nanocrystalline NiTi Intermetallic Alloy Wire

Jeremy E. Schaffer

(Submitted October 8, 2008; in revised form December 3, 2008)

Homogeneous 177- μm diameter nanocrystalline Nitinol wires were produced and compared to microcrystalline Nitinol from equivalent ingot stock. Property measurement was carried out using cyclic tension testing, strain-controlled fatigue testing and bend and stress-free recovery testing (BFR). A B2 cubic structure of 5- to 60-nm grain size was confirmed by transmission electron microscopy (TEM). The fatigue strain capability at 10^7 cycles is 30% greater in the nanocrystalline versus microcrystalline annealed wire. Grain size and residual strain are positively correlated in cyclic uniaxial tension testing within the super-elastic temperature and strain regime. A transformation-induced loading plateau that is 40% longer than in standard superelastic polycrystalline wire is also reported for the first time.

Keywords long-plateau Nitinol, medical wire, nanocrystalline Nitinol, Nitinol processing, Nitinol wire

1. Introduction

Nitinol medical devices are designed with functional shapes which are driven into living anatomy through tiny incisions, forced through millimeter scale conduit and finally thermally or mechanically placed to function and ideally enhance the life of the patient in a mechanically and chemically dynamic biological flora. It is critical that medical device engineers have the proper tools to discern optimal design with Nitinol including knowledge of relevant microstructural-property relationships.

Grain size has been known as an important variable in defining material strength, fracture toughness, and fatigue strength since the pioneering work of E.O Hall and N.J. Petch in the late 1940s (Ref 1). In fine wire structural applications, such as medical lead wire assemblies, coarse microstructure in Co-Ni-Cr alloys has been shown to negatively impact mechanical fatigue performance (Ref 2).

Researchers have recently begun to recognize the unique properties of ultra fine-grained (UFG) metals (Ref 3, 4). Pelton and colleagues first reported UFG Nitinol in 1986 during in situ crystallization of amorphized Nitinol thin films (Ref 5). UFG Nitinol studies have become more common in the primary literature since this pioneering work. Sun and Li reported on the unique phase transformation and localization in nano-grained

1-1.5 mm diameter Nitinol microtubes (Ref 6). Sergueeva et al. presented an in depth study of the nanocrystallization process in 12 mm Nitinol disks, which underwent amorphization by severe plastic deformation (SPD) (Ref 7). Others researchers (Ref 8-12) have examined certain aspects of nanostructure generation and properties, while few have examined detailed structure-function relationships in fine (less than 250 μm diameter) Nitinol wire over a range of grain sizes from nanometers to micrometers. The goal of this study was to begin to quantify the grain size effect at fine wire diameters, which are of increasing importance in medical device design for example in self-expanding stents, blood filters, and tissue scaffold platforms.

2. Experimental

Approximately 2 mm Nitinol wire with an ingot A_5 of 243 K, comprising Ti-50.9 at.% Ni was equivalently drawn and annealed to a diameter of 230 μm . At this stage, wires were continuously strand annealed at 923-1123 K at a sufficient dwell time to ensure complete recrystallization with a nominally 2- μm grain size. Samples were subsequently wet-drawn using natural diamond drawing dies and oil-based lubricants to a finish diameter of 177 μm with nominally 40% retained cold work. Wires were then continuously annealed at constant stress for less than 60s to effect recrystallization while minimizing potential Ni-rich precipitate formation.

Near-surface microstructure and oxide thickness determination was performed using thin foil preparation and extraction by focused ion beam (FIB, FEI Nova 200 NanoLab) and transmission electron microscopy (TEM, JEOL 2000EX, 200 keV). The preparation method is represented in Fig. 1. The targeted sample surface is initially masked with a thin layer of vapor platinum compound deposit to protect the surface from ion implantation damage (Ref 13). Grain size distributions were calculated using digital image analysis (ImageJ 1.40f, National Institutes of Health, USA) as shown schematically in Fig. 2.

Active sample transformation temperatures were analyzed using bend and free recovery (BFR) methodology using a

This article is an invited paper selected from presentations at Shape Memory and Superelastic Technologies 2008, held September 21-25, 2008, in Stressa, Italy, and has been expanded from the original presentation.

Jeremy E. Schaffer, Fort Wayne Metals Research Products Corporation, 9609 Ardmore Avenue, 46809 Fort Wayne, IN; and **Jeremy E. Schaffer**, Weldon School of Biomedical Engineering, Purdue University, 47906 West Lafayette, IN. Contact e-mail: jeremy_schaffer@fwmetals.com.

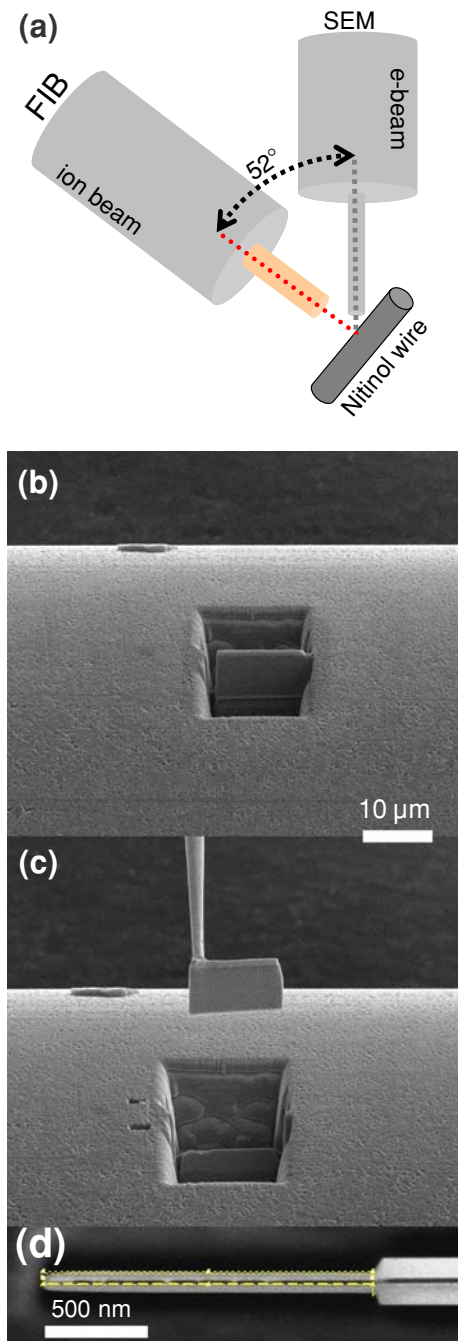


Fig. 1 (a) Schematic of dual beam SEM/FIB equipment used for thin foil TEM sample preparation, gallium ion source for milling is targeted at a common eucentric height shared by the electron beam for imaging. Gallium ions are accelerated using a 30 kV potential and electromagnetically focused to an area that can be controlled by feedback image data gathered from the far less damaging scanning electron beam. (b) Cross section “rough” cuts to expose lift out foil at a nominal thickness of 1000 nm. (c) Foil lift out using a 2- μm tungsten probe. (d) After attachment to a SEM grid post, sample is thinned at reduced ion current to a thickness of about 100 nm or less

proprietary digital video analysis apparatus per standard ASTM F2082-06 (Ref 14). Cyclic and monotonic uniaxial tensile properties were measured at an ambient temperature of 298 K at a strain rate of 10^{-3} s^{-1} using an Instron Model 5565 Tensile Test Bench equipped with pneumatic grips. Fatigue behavior

was characterized using rotary beam fatigue test equipment manufactured by Positool, Inc. at 3600 r/min in ambient 298 K air. Specimens from each grain size condition were tested at alternating strain levels ranging from 0.5 to 2.5% to a maximum of about 10^8 cycles.

3. Results and Discussion

3.1 Microstructural Data

Nitinol wire was successfully produced at 177 μm diameter with many levels of grain nucleation and growth. Five distinct microstructures were chosen for subsequent thermomechanical and structural fatigue testing comprising median grain sizes of: 50 nm, 100 nm, 2 μm , 5 μm , and 10 μm . Selected area electron diffraction patterns were acquired in order to observe texture states and to look for evidence of precipitate reflections, an example of which is shown in Fig. 2(d-f). No evidence of lenticular precipitates was found in the diffraction data.

The nanocrystalline samples were confirmed to be homogeneous within the first 10 μm of material below the drawn oxide surface using TEM. Observed grain structures are presented in Fig. 3. Empirical cumulative distribution functions were plotted for each grain size as given in Fig. 4. Average oxide thickness for all samples was found to be about 120 nm, an example of which is given in Fig. 5. Further experimentation is underway to understand microstructure along the central portion of the wires.

3.2 Transformation Temperatures

Active transformation temperatures were measured using BFR methods in accordance with ASTM standard F2082. All samples analyzed exhibited an A_s temperature of $240 \pm 5 \text{ K}$, in good agreement with ingot DSC data. Plots of recovery data for each sample are given in Fig. 6. The samples that possessed equiaxed grain sizes greater than 100 nm showed a clear single stage transformation associated with recovery from the martensitic to austenitic structure, and an active A_f of $250 \pm 5 \text{ K}$. At the 50-nm grain size, samples exhibited a right-shifted recovery. The assumption of an entirely austenitic transformation placed calculations for the A_f of the 50 nm samples at 277-279 K. Further data is needed, particularly in situ TEM analysis, to provide a mechanistic description of this behavior. The extended thermal recovery may be related to high levels of strain energy stored in the nanocrystalline material due to a relatively large grain-boundary density. Martensite variant activity may also differ in the nanostructures during recovery, which could lead to distinct behavior in BFR testing.

3.3 Tensile Testing

The evolution of axial properties as a function of grain size followed a path expected from the classic Hall-Petch relationship: fine-grained material exhibited increased strength and reduced plasticity during cyclic testing. Single cycle uniaxial tension testing to a reversal point of 4% strain showed a positive correlation between grain size and isothermal residual strain, defined by the residual strain after load release without raising sample temperature. This relationship is shown in Fig. 7(c). The ultimate tensile strength measured in axial monotonic tension testing increased with reduced grain size as shown in Fig. 7(d).

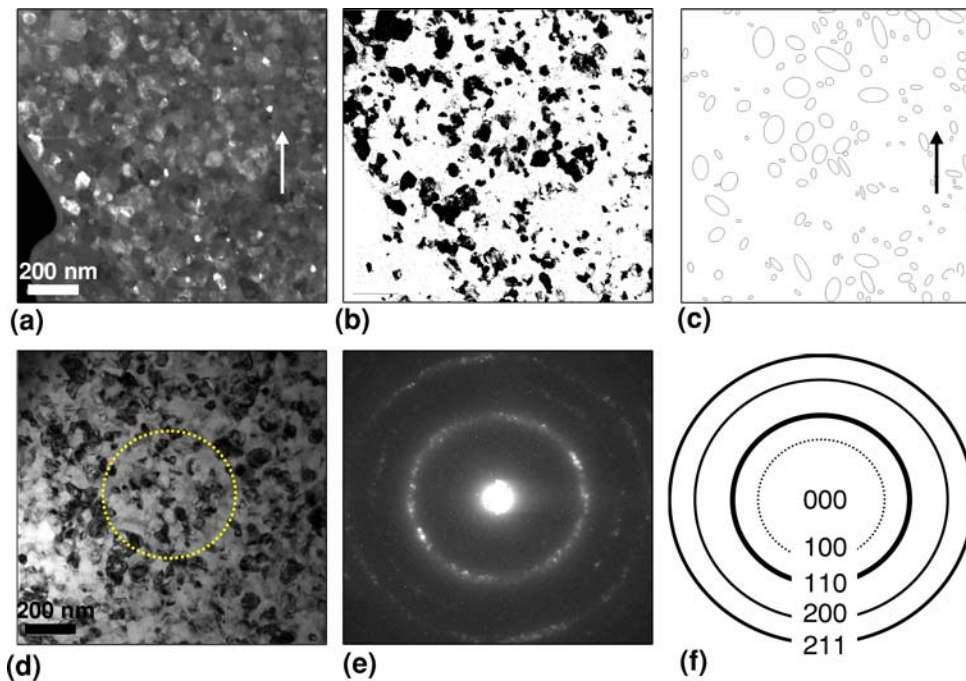


Fig. 2 (a) Dark field (DF) TEM image of sample with median 50-nm grain size. (b) Binary conversion of preceding DF-TEM image for digital grain size analysis. (c) Ellipsoidal representation of analyzed grain field showing lack of residual grain elongation in the drawing (arrow) direction. (d) Bright field (BF) TEM image of equivalent material (different area). (e) Selected area diffraction pattern (SADP) of area shown in (d) showing bright B2 cubic (110) polycrystalline ring. (f) Calculated powder DP for B2 Nitinol

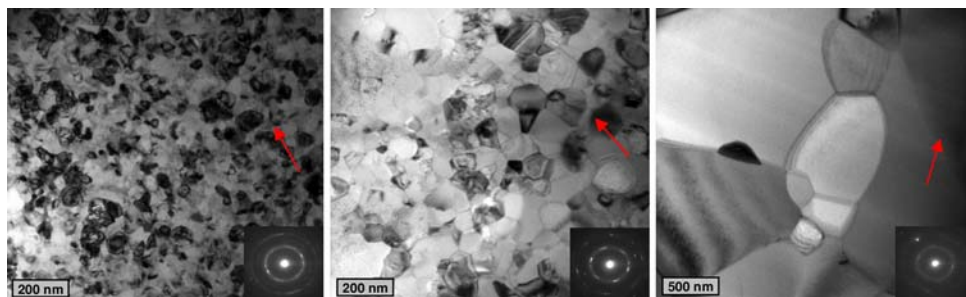


Fig. 3 BF-TEM images showing three of five examined grain sizes, left to right median sizes: 50 nm, 100 nm, 2 μ m. Red arrow indicates wire drawing direction. All samples were found to possess equiaxed microstructure with little apparent signature from remnant cold work. Of note, the dark fringes in the far right image are associated with Moire interference and tilt grain-boundary thickness fringes (Ref 15)

The initial onset of isothermally recoverable transformation strain and significant reversion stress at the 2- μ m grain size was attributed to a reduction in the irreversible plastic behavior during stress-induced transformation. The finer, more plasticity resistant microstructures were not as susceptible to the stabilization of martensite by dislocation network formation. This behavior was consistent with the discussion by Duerig in Ref 16.

A large increase in both ultimate and unloading plateau strength was found in the samples comprising 100 and 50-nm grain sizes, respectively. Waitz et al. found competing accommodation mechanisms in martensitic NiTi, with single variant B19' plates forming below about 80 nm and compound twinned variants forming in grains larger than about 100 nm (Ref 17). A similar grain size threshold mechanism may contribute to constitutive behavior differences found in the present samples.

The length of the stress-induced martensite load plateau was found to vary with the microstructural state. Figure 7(b) shows

a typical superelastic plateau; the onset of elastic loading of the B19' matrix occurred at 7% strain. In the precipitate-free structure with a 100-nm equiaxed grain size, the transformation plateau terminated at 10.1% strain, with 9.6% strain recovery upon isothermal unloading. Theoretical recoverable strains as high as 10.5% have been calculated in preferred transformation orientations such as [123] by Sehitoglu et al. in Ref 18. Until now, near-theoretical strain recovery has not been observed in isothermal tension testing of fine wire samples. The long-plateau behavior observed here is likely related to favorable texture that was not apparent in the present electron diffraction data sets. One limiting factor that should be resolved is the small amount of analyzed surface material; understanding of full section texture will be critical going forward. Further texture measurement is underway aimed at providing a mechanistic description of the long-plateau phenomenon.

Residual stress distributions on the microstructural level have been shown to provide B19' phase stabilization (Ref 19).

It is possible that grain constraint effects in the nanocrystalline regime are another important factor in determining initial phase distributions, transformation paths, and overall constitutive behavior. It is unknown whether this could impact effective transformation plateau length.

As shown in Fig 7(a), the unloading stiffness was found to decrease significantly from a nearly grain-size-invariant 42 GPa to 29 GPa at the 50-nm grain size. In 2006, Duerig demonstrated a similar unloading modulus range for various strain values and gave some explanation related to anelastic reversion of detwinned martensite (Ref 16). Here we see variability as a function of grain size with step behavior between 50 and 100 nm. This behavior may be the result of energetic competition between single and compound martensite variants and will require in situ TEM deformation studies for further illumination. If properly controlled, this discovery could be meaningful in the context of a wire stent in a pulsating blood vessel where relative implant stiffness is known to affect overall device performance (Ref 20, 21).

3.4 Fatigue Testing

Rotary beam fatigue test results show increased damage accumulation rates with increasing grain size. This was particularly evident under conditions where lives were on the

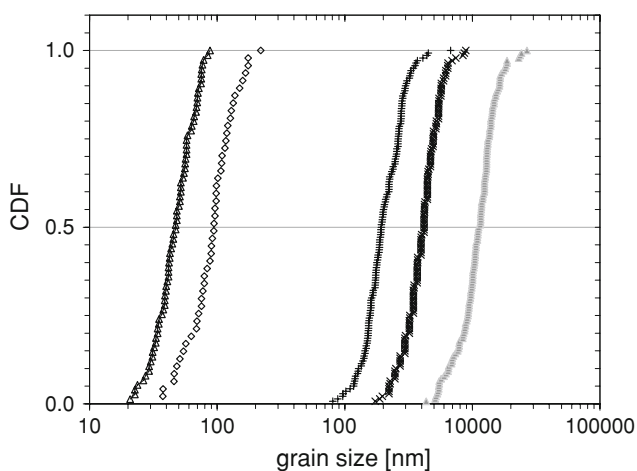


Fig. 4 Cumulative distribution function representation of grain size distributions for, median grain sizes, left to right: 50, 100, 2000, 5000, and 10000 nm

order of 10^5 - 10^7 cycles. Figure 8(a) shows strain-life curves for each material. Wire with a 50-nm grain size resisted fracture at the 0.9% alternating strain to beyond 10^7 cycles. At a 10- μ m grain size, the 10^7 cycle strain level was 0.6%; other grain sizes fell in order between these values with coarse structures yielding reduced resistance to damage (Fig. 8b).

4. Conclusions

1. Isothermal recoverable strains of 9.6%, greater than 90% of the theoretical limit, were measured in nanocrystalline Nitinol wire.
2. Zero residual strain in a 4% strain cycle was observed in an equiaxed, precipitate-free, and untrained material with a median 50-nm grain size.
3. A 30% increase in fatigue damage resistance was observed in nanocrystalline versus microcrystalline wire.
4. Thermally extended recovery during BFR testing was found in samples with a median grain size less than about 100 nm.
5. The unloading stiffness was found to decrease stepwise from 42 GPa to 29 GPa moving from 100 nm to the 50-nm grain size.

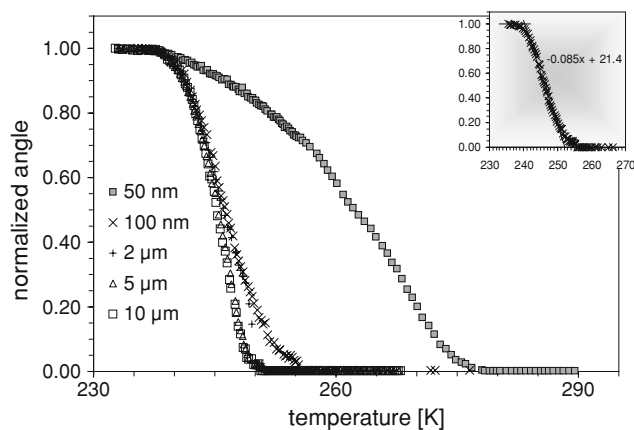


Fig. 6 Digital vision BFR test data for five distinct grain sizes. It is postulated that active austenitic finish temperature shift is due to the relatively high grain-boundary content in the nanocrystalline material

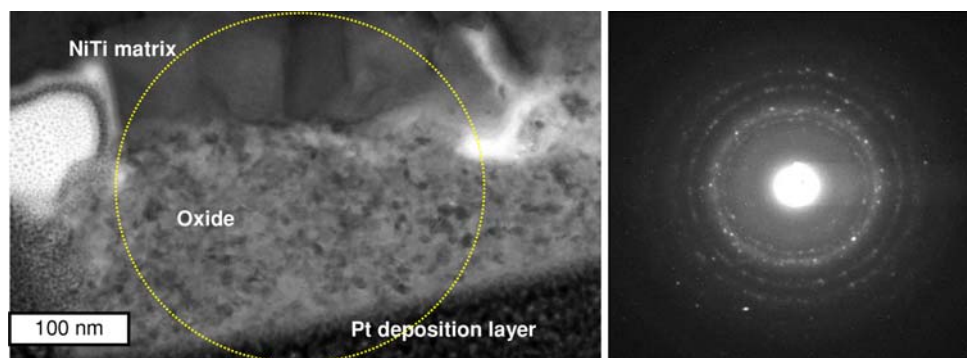


Fig. 5 (left) NiTi oxide layer. (right) SADP taken from the indicated area showing powder diffraction rings associated with nanocrystalline oxide

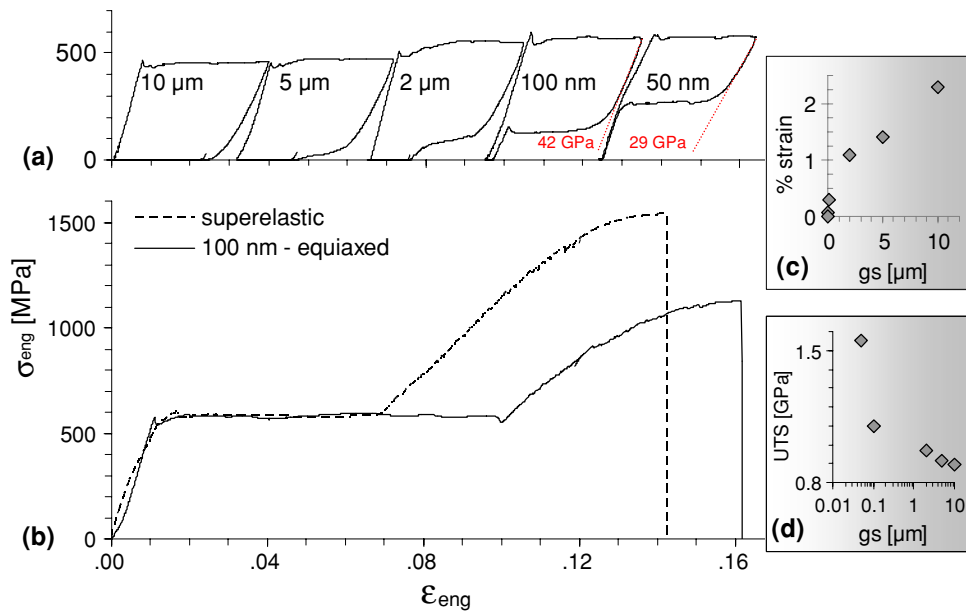


Fig. 7 Engineering stress-strain data ran at a temperature of 298 K in quiescent air at a strain rate of 10^{-3} s^{-1} . (a) 4% hysteresis loops as a function of equiaxed grain size. Unloading moduli and values shown in red; (b) monotonic loading curves for standard superelastic material and wire with a homogeneous 100 nm, precipitate-free matrix; (c) residual strain as a function of grain size; (d) ultimate tensile strength as a function of grain size

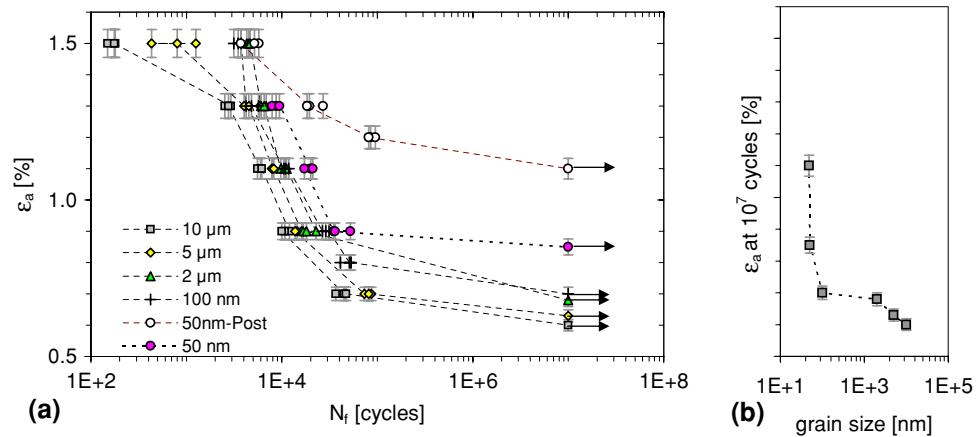


Fig. 8 (a) Strain-life representation of rotary beam fatigue data. Test conditions: $R = -1$, $T = 298 \text{ K}$, $f = 60 \text{ s}^{-1}$, environment: quiescent air, $N = 5$ at each strain level. (b) Strain limit at 10^7 cycles. Note: pictured with maximum strain level error of $\pm 3\%$, cycle count error $< 0.1\%$

Acknowledgments

The author gratefully acknowledges the staff of Fort Wayne Metals for providing financial support to this project. Special thanks also go to David Snider, Mike McGuire, Dave Plumley, and Chris Hoffman for help with material and data acquisition.

References

1. E.O. Hall, The Deformation and Ageing of Mild Steel: III Discussion of Results, *Proc. Phys. Soc. B*, 1951, **64**, p 747–753
2. J.E. Schaffer, “A Hierarchical Initiation Mechanism Approach to Modeling Fatigue Life Variability in 35Co–35Ni–20Cr–10Mo Medical Grade Fine Wire”, Master of Science in Mechanical Engineering Thesis Manuscript, Purdue University, West Lafayette, IN, 2007
3. T. Hanlon, E.D. Tabachnikova, and S. Suresh, Fatigue Behavior of Nanocrystalline Metals and Alloys, *Int. J. Fatigue*, 2005, **27**, p 1147–1158
4. H.W. Hoepfel, M. Kautz, C. Xu, M. Murashkin, T.G. Langdon, R.Z. Valiev, and H. Mughrabi, An Overview: Fatigue Behaviour of Ultrafine-Grained Metals and Alloys, *Int. J. Fatigue*, 2006, **28**, p 1001–1010
5. A. Pelton, P. Moine, M.A. Noack, and R. Sinclair, Crystalline-to-Amorphous Transitions in Ti-Ni Alloys, *Mater. Res. Soc. Symp. Proc.*, 1986, **62**, p 291–302
6. Q.P. Sun and Z.Q. Li, Phase Transformation in Superelastic NiTi Polycrystalline Micro-tubes Under Tension and Torsion from Localization to Homogeneous Deformation, *Int. J. Solids Struct.*, 2002, **39**, p 3797–3809
7. A.V. Sergueeva, C. Song, R.Z. Valiev, and A.K. Mukherjee, Structure and Properties of Amorphous and Nanocrystalline NiTi Prepared by Severe Plastic Deformation and Annealing, *Mater. Sci. Eng. A*, 2003, **339**, p 159–165

8. X. Xu and N. Thadhani, Shock Synthesis and Characterization of Nanostructured Nitinol Alloy, *Mater. Sci. Eng. A*, 2004, **384**, p 194–201
9. P.L. Potapov, W. Tirry, and D. Schryvers, Cross-section Transmission Electron Microscopy Characterization of the Near-surface Structure of Medical Nitinol Superelastic Tubing, *J. Mater. Sci.: Mater. Med.*, 2007, **18**, p 483–492
10. T. Mousavi, F. Karimzadeh, and M.H. Abbasi, Synthesis and Characterization of Nanocrystalline NiTi Intermetallic by Mechanical Alloying, *Mater. Sci. Eng. A*, 2008, **487**, p 46–51
11. T. Sawaguchi, G. Kustraeter, A. Yawny, M. Wagner, and G. Eggeler, Crack Initiation and Propagation in 50.9 at. pct Ni-Ti Pseudoelastic Shape-memory Wires in Bending-rotation Fatigue, *Metal. Mater. Trans. A*, 2003, **34**, p 2847–2860
12. G. Eggeler, E. Hornbogen, A. Yawny, A. Heckmann, and M. Wagner, Structural and Functional Fatigue of NiTi Shape Memory Alloys, *Mater. Sci. Eng. A*, 2004, **378**, p 24–33
13. W.Y. Kwong and W.Y. Zhang, Electron-beam Assisted Platinum Deposition as a Protective Layer for FIB and TEM Applications, *Proceedings of IEEE International Symposium on Semiconductor Manufacturing*, ISSM September, IEEE, New York, NY, USA, p 469–471
14. ASTM F2082-06, Standard Test Method for Determination of Transformation Temperature of Nickel-Titanium Shape Memory Alloys by Bend and Free Recovery, in *Annual Book of Standards*, ASTM International, Philadelphia, PA, 2006, p 1–7
15. D.B. Williams and C.B. Carter, *Transmission Electron Microscopy III Imaging*, Springer Science + Business Media, LLC, New York, NY, USA, 1996, p 444–450
16. T.W. Duerig, Some Unsolved Aspects of Nitinol, *Mater. Sci. Eng. A*, 2006, **438–440**, p 69–74
17. T. Waitz, W. Pranger, T. Antretter, F.D. Fischer, and H.P. Karnthaler, Competing Accommodation Mechanisms of the Martensite in Nanocrystalline NiTi Shape Memory Alloys, *Mater. Sci. Eng. A*, 2008, **481–482**, p 479–483
18. H. Sehitoglu, R. Hamilton, D. Canadinc, X.Y. Zhang, K. Gall, I. Karaman, Y. Chumlyakov, and H.J. Maier, Detwinning in NiTi Alloys, *Metal. Mater. Trans. A*, 2003, **34**, p 5–13
19. X. Huang, G.J. Ackland, and K.M. Rabe, Crystal Structures and Shape-Memory Behaviour of NiTi, *Nat. Mater.*, 2003, **2**, p 307–311
20. J. Black, *Biological Performance of Materials*, 4th ed., CRC Press Taylor & Francis Group, Boca Raton, FL, USA, 2006, p 195–205
21. D. Stoeckel, A. Pelton, and T. Duerig, Self-expanding Nitinol Stents: Material and Design Considerations, *Eur. Radiol.*, 2004, **14(2)**, p 292–301